

Modal Analysis Based on an Integral Equation Method for Characterizing Wireless Channels in a Fully-Enclosed Environment

Xin Wang¹, Han Cheng¹, Xuemei Cao¹,
Chen Chen¹, and Mingyu Lu^{2, *}

Abstract—Wireless communication and/or wireless power transmission are highly desired in some of the practical environments fully enclosed by conducting walls. In this paper, a semi-analytical modal analysis is conducted for the purpose of characterizing wireless channels in a fully-enclosed space. The modal analysis is based upon an integral equation method. The cavity Green’s function in the spectral domain (that is, expressed in term of cavity modes) is employed in the integral equation. The analysis results indicate that when a transmitter and a receiver are symmetric to each other with respect to a certain cavity mode, the load of the receiver could be coupled to the transmitter with little dispersion, leading to excellent wireless channels with the potential of accomplishing efficient wireless communication and/or wireless power transmission. A cubic cavity with a side length of 1 meter is analyzed as a specific example, and the modal analysis results are verified by experiments. Measurement data agree with the theoretical analysis very well. As predicted by the theoretical analysis, excellent wireless channels associated with the TM_{220} mode (with a bandwidth of 40 MHz), TM_{310} mode (with a bandwidth of 10 MHz), and TM_{311} mode (with a bandwidth of 20 MHz) are demonstrated inside a cubic box with a side length of 1 meter.

1. INTRODUCTION

In some practical environments fully enclosed by conducting walls, such as space stations, man-made satellites, submarines, and aircrafts, wireless communication, and/or wireless power transmission are highly desired. For instance, the operation of man-made satellite relies on a network of distributed sensors, and due to space and weight constraints, the sensors are desired to transmit data without wired connections [1]; meanwhile, battery life constitutes a bottleneck of the wireless sensors, and thus delivering power wirelessly to the sensors would improve the performance of wireless sensor network tremendously [2]. Because of the rich multi-path propagation in fully-enclosed space, high-speed wireless communication has been considered a challenging task [3, 4]. Numerous research efforts have been reported on characterizing wireless communication channels in fully-enclosed environments by the means of simulations and/or measurements [5–12]. The results in [5–12] unequivocally reveal highly-dispersive wireless channels, which make it difficult for the data rate of wireless communication to reach Mbps. In recent years, wireless power transmission in fully-enclosed environments is investigated by many researchers [13–15]. Since electromagnetic fields in fully-enclosed environments exhibit strong standing wave patterns, wireless power transmission is sensitive to the spatial location. When a wireless power receiver is located at certain “bright spots,” power transmission efficiency could approach 100% [2]; whereas there may exist “dark spots” at which a wireless power receiver receives little power. Several

Received 10 September 2019, Accepted 17 December 2019, Scheduled 31 January 2020

* Corresponding author: Mingyu Lu (mingyu.lu@mail.wvu.edu).

¹ College of Electronic and Information Engineering, Nanjing University of Aeronautics and Astronautics, Nanjing, Jiangsu 211106, China. ² Department of Electrical and Computer Engineering, West Virginia University Institute of Technology, Beckley, West Virginia 25801, USA.

techniques, including taking advantage of mechanical stirring [16], multiple frequencies [17], and parasitic elements [18], have been proposed to avoid “dark spots” of wireless power transmission.

In this paper, a semi-analytical modal analysis is conducted for the purpose of characterizing wireless channels in fully-enclosed space. Compared with the approaches in [2–18], the semi-analytical modal analysis is capable of yielding explicit physical insights toward efficient wireless communication and/or wireless power transmission in fully-enclosed environments. Specifically, the modal analysis is based upon an integral equation method. The cavity Green’s function in the spectral domain (that is, expressed in term of cavity modes) is employed in the integral equation. In a cubic cavity with a side length of 1 meter, the frequency band around 424 MHz (which is the resonant frequency of the TM_{220} mode in the cubic cavity) is analyzed comprehensively. The analysis results reveal that when a transmitter and a receiver are symmetric to each other as far as TM_{220} mode is concerned, the load of the receiver could be coupled to the transmitter with little dispersion, leading to an excellent wireless communication channel in which the amplitude spectrum of transfer function is flat and the phase spectrum of transfer function is linear with respect to frequency around the resonant frequency of TM_{220} mode. Moreover when the transmitter and receiver reside at certain spatial spots, the channel exhibits power transmission efficiency higher than 70%, making it a good candidate for wireless power transmission. Theoretical derivations further indicate that it is possible to identify excellent wireless channels (with the potential of accomplishing efficient wireless communication and/or wireless power transmission) associated with modes other than the TM_{220} mode.

The modal analysis is verified by experiments in the frequency domain as well as time domain. Measurement data inside a cubic box, which emulates a man-made satellite, agree with the theoretical analysis very well. Excellent wireless communication channels approximately between 395 MHz and 435 MHz, with an absolute bandwidth as large as 40 MHz, are demonstrated. Based on the measurement data, these channels have the potential of accommodating wireless communication with data rate of at least 20 Mbps. The power transmission efficiency is greater than 70% in the frequency range of [395 MHz, 435 MHz] when the receiver is located at certain “bright spots.” At certain “dark spots,” the receiver receives little power but wireless communication with data rate of 20 Mbps still appears feasible. Two other excellent wireless channels are also demonstrated by measurements as predicted by the theoretical analysis: one associated with TM_{310} mode with 10 MHz bandwidth, and one associated with TM_{311} mode with 20 MHz bandwidth.

The rest of this paper is organized as follows. Section 2 describes the modal analysis and its theoretical results. Experimental verifications are presented in Section 3. Finally, Section 4 relates to our conclusions.

2. MODAL ANALYSIS FOR CHARACTERIZING WIRELESS CHANNELS IN A RECTANGULAR CAVITY

In this section, a modal analysis based upon the integral equation method is conducted for characterizing wireless channels inside a rectangular cavity. The theoretical setup is illustrated in Figure 1. A cubic cavity, which emulates man-made satellites, has a side length of 1 meter and its six walls are all made of perfect conductors. There is only air inside the cavity except one transmitting probe and one receiving probe. Both the transmitting and receiving probes are thin wires oriented along z direction, behaving as monopole antennas. The two probes are assumed to have the same length l_p and same radius r_p . The transmitting and receiving probes are terminated at $z = 0$ plane by co-axial connectors, which are defined as port 1 and port 2 respectively. The transmitting probe and receiving probe are located at $(x = x_t, y = y_t)$ and $(x = x_r, y = y_r)$, respectively.

An equivalent problem corresponding to the setup of Figure 1 is constructed in Figure 2. The cavity is fully enclosed by perfect conducting walls. Electric surface currents \mathbf{J}_t and \mathbf{J}_r reside at $(x = x_t, y = y_t)$ and $(x = x_r, y = y_r)$ respectively, extended along the z direction. Because the probes in Figure 1 are thin with respect to the wavelength, \mathbf{J}_t and \mathbf{J}_r are assumed to have a z component only. Magnetic surface currents \mathbf{M}_t and \mathbf{M}_r reside around $(x = x_t, y = y_t)$ and $(x = x_r, y = y_r)$ respectively, corresponding to the co-axial openings in Figure 1 [19]. An electric field integral equation can be formulated from

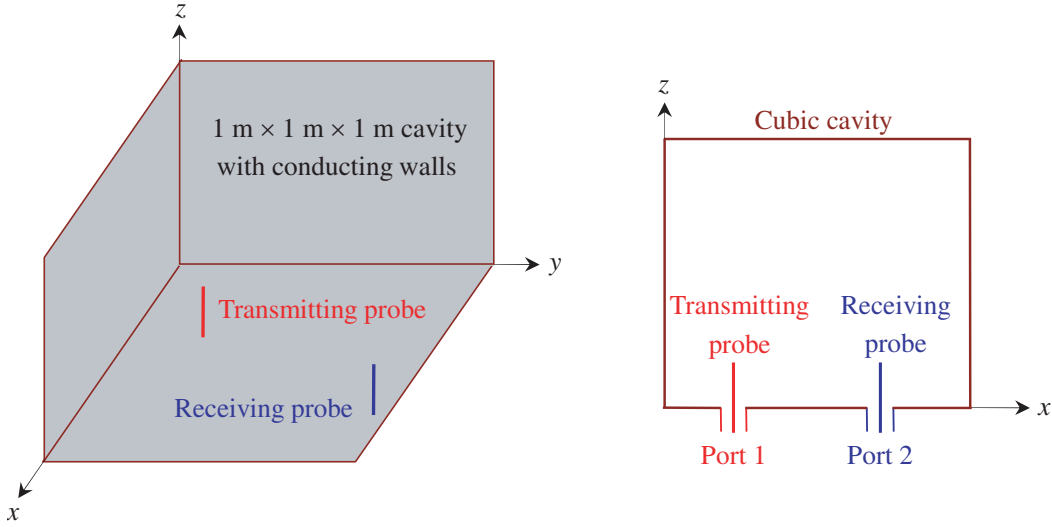


Figure 1. Illustration of the theoretical setup.

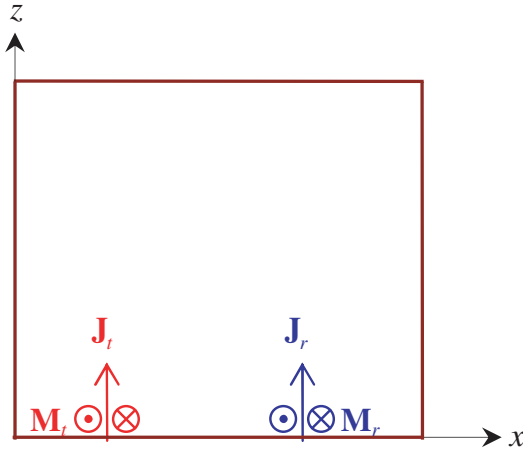


Figure 2. Equivalent problem corresponding to the setup of Figure 1.

Figure 2.

$$\hat{\mathbf{z}} \cdot \int \bar{\mathbf{G}}_{EM}(\mathbf{r}, \mathbf{r}') \cdot [\mathbf{M}_t(\mathbf{r}') + \mathbf{M}_r(\mathbf{r}')] d\mathbf{r}' + \hat{\mathbf{z}} \cdot \int \bar{\mathbf{G}}_{EJ}(\mathbf{r}, \mathbf{r}') \cdot [\mathbf{J}_t(\mathbf{r}') + \mathbf{J}_r(\mathbf{r}')] d\mathbf{r}' = 0, \quad (1)$$

when \mathbf{r} is on probe surface.

Equation (1) enforces that the tangential electric field over probe surface is zero. The electric field in Figure 2 is generated by four sources: \mathbf{J}_t , \mathbf{J}_r , \mathbf{M}_t , and \mathbf{M}_r . In Eq. (1), $\bar{\mathbf{G}}_{EM}$ and $\bar{\mathbf{G}}_{EJ}$ are dyadic Green's functions of the rectangular cavity, with $\mathbf{r} = (x, y, z)$ denoting the field position and $\mathbf{r}' = (x', y', z')$ denoting the source position. To be more specific, $\bar{\mathbf{G}}_{EM}(\mathbf{r}, \mathbf{r}')$ prescribes the electric field at \mathbf{r} due to a magnetic current dipole at \mathbf{r}' , and $\bar{\mathbf{G}}_{EJ}(\mathbf{r}, \mathbf{r}')$ prescribes electric field at \mathbf{r} due to an electric current dipole at \mathbf{r}' . Electric currents \mathbf{J}_t and \mathbf{J}_r only have a z component; the magnetic currents \mathbf{M}_t and \mathbf{M}_r only have x component and y component; and Equation (1) only requires calculating the z component of the electric field. Based on the above facts, the following three components of dyadic

Green's functions $\bar{\mathbf{G}}_{EM}$ and $\bar{\mathbf{G}}_{EJ}$ are needed in Eq. (1).

$$\hat{\mathbf{z}} \cdot \bar{\mathbf{G}}_{EM}(\mathbf{r}, \mathbf{r}') \cdot \hat{\mathbf{x}} = \frac{8}{abd} \sum_{m=1}^{\infty} \sum_{n=1}^{\infty} \sum_{p=0}^{\infty} \frac{1}{\xi_p} \frac{k_{y,n}}{k^2 - (k_{mnp})^2} \cdot \sin(k_{x,m}x) \sin(k_{y,n}y) \cos(k_{z,p}z) \sin(k_{x,m}x') \cos(k_{y,n}y') \cos(k_{z,p}z') \quad (2)$$

$$\hat{\mathbf{z}} \cdot \bar{\mathbf{G}}_{EM}(\mathbf{r}, \mathbf{r}') \cdot \hat{\mathbf{y}} = \frac{8}{abd} \sum_{m=1}^{\infty} \sum_{n=1}^{\infty} \sum_{p=0}^{\infty} \frac{1}{\xi_p} \frac{-k_{x,m}}{k^2 - (k_{mnp})^2} \cdot \sin(k_{x,m}x) \sin(k_{y,n}y) \cos(k_{z,p}z) \cos(k_{x,m}x') \sin(k_{y,n}y') \cos(k_{z,p}z') \quad (3)$$

$$\hat{\mathbf{z}} \cdot \bar{\mathbf{G}}_{EJ}(\mathbf{r}, \mathbf{r}') \cdot \hat{\mathbf{z}} = \frac{1}{j\omega\epsilon_0} \frac{8}{abd} \sum_{m=1}^{\infty} \sum_{n=1}^{\infty} \sum_{p=0}^{\infty} \frac{1}{\xi_p} \frac{(k_{z,p})^2 - k^2}{k^2 - (k_{mnp})^2} \cdot \sin(k_{x,m}x) \sin(k_{y,n}y) \cos(k_{z,p}z) \sin(k_{x,m}x') \sin(k_{y,n}y') \cos(k_{z,p}z') \quad (4)$$

The expressions in Eqs. (2) to (4) follow the classic eigenfunction expansion derivations in [20]. Time dependence $e^{j\omega t}$ is suppressed with $j = \sqrt{-1}$; $\omega = 2\pi f$ is the angular frequency; f is the operating frequency; a , b , and d are the cavity dimensions along x , y , and z axes respectively (in all the theoretical and experimental examples of this paper, $a = b = d = 1$ meter); $\xi_0 = 2$, and $\xi_p = 1$ when $p \neq 0$; $k = \omega\sqrt{\epsilon_0\mu_0}$ is the wavenumber in free space; ϵ_0 and μ_0 are the permittivity and permeability of free space respectively; and $k_{mnp} = \sqrt{(k_{x,m})^2 + (k_{y,n})^2 + (k_{z,p})^2}$, with $k_{x,m} = m\pi/a$, $k_{y,n} = n\pi/b$, and $k_{z,p} = p\pi/d$.

With k_{mnp} denoting the wavenumber associated with mode (m, n, p) of the rectangular cavity, $f_{mnp} = k_{mnp}/(2\pi\sqrt{\epsilon_0\mu_0})$ is used to denote the resonant frequency associated with mode (m, n, p) . As the finding of this research, it is possible to identify excellent wireless channels when the operating frequency f is around $f_{m^*n^*p^*}$, the resonant frequency of a specific mode (m^*, n^*, p^*) . In this section, the TM_{z220} mode is studied as a specific example. In other words, in this section it is assumed that $f \rightarrow f_{m^*n^*p^*}$ (that is, f approaches $f_{m^*n^*p^*}$) with $m^* = 2$, $n^* = 2$, and $p^* = 0$. With $m^* = 2$, $n^* = 2$, and $p^* = 0$, the resonant frequency $f_{m^*n^*p^*}$ is approximately 424 MHz. When f approaches $f_{m^*n^*p^*}$ (which is equivalent to k approaching $k_{m^*n^*p^*}$), mode (m^*, n^*, p^*) dominates the fields inside the cavity. Mathematically speaking, the terms associated with indices (m^*, n^*, p^*) are outstanding in Eqs. (2) to (4). By defining $u^* = k^2 - (k_{m^*n^*p^*})^2$ and multiplying u^* onto Eq. (1), it is not difficult to find that when $f \rightarrow f_{m^*n^*p^*}$

$$Q^* = k_{y,n^*} \left[(\tilde{M}_t)_{x,m^*n^*p^*} + (\tilde{M}_r)_{x,m^*n^*p^*} \right] - k_{x,m^*} \left[(\tilde{M}_t)_{y,m^*n^*p^*} + (\tilde{M}_r)_{y,m^*n^*p^*} \right] + \frac{(k_{z,p^*})^2 - k^2}{j\omega\epsilon_0} \left[(\tilde{J}_t)_{z,m^*n^*p^*} + (\tilde{J}_r)_{z,m^*n^*p^*} \right] \rightarrow 0, \quad (5)$$

where

$$(\tilde{M}_t)_{x,m^*n^*p^*} = \int \hat{\mathbf{x}} \cdot \mathbf{M}_t(\mathbf{r}') \sin(k_{x,m^*}x') \cos(k_{y,n^*}y') \cos(k_{z,p^*}z') d\mathbf{r}', \quad (6)$$

$$(\tilde{M}_r)_{x,m^*n^*p^*} = \int \hat{\mathbf{x}} \cdot \mathbf{M}_r(\mathbf{r}') \sin(k_{x,m^*}x') \cos(k_{y,n^*}y') \cos(k_{z,p^*}z') d\mathbf{r}', \quad (7)$$

$$(\tilde{M}_t)_{y,m^*n^*p^*} = \int \hat{\mathbf{y}} \cdot \mathbf{M}_t(\mathbf{r}') \cos(k_{x,m^*}x') \sin(k_{y,n^*}y') \cos(k_{z,p^*}z') d\mathbf{r}', \quad (8)$$

$$(\tilde{M}_r)_{y,m^*n^*p^*} = \int \hat{\mathbf{y}} \cdot \mathbf{M}_r(\mathbf{r}') \cos(k_{x,m^*}x') \sin(k_{y,n^*}y') \cos(k_{z,p^*}z') d\mathbf{r}', \quad (9)$$

$$(\tilde{J}_t)_{z,m^*n^*p^*} = \int \hat{\mathbf{z}} \cdot \mathbf{J}_t(\mathbf{r}') \sin(k_{x,m^*}x') \sin(k_{y,n^*}y') \cos(k_{z,p^*}z') d\mathbf{r}', \quad (10)$$

$$(\tilde{J}_r)_{z,m^*n^*p^*} = \int \hat{\mathbf{z}} \cdot \mathbf{J}_r(\mathbf{r}') \sin(k_{x,m^*}x') \sin(k_{y,n^*}y') \cos(k_{z,p^*}z') d\mathbf{r}'. \quad (11)$$

As the physical meaning of Eq. (5), the sum of all the sources' projections onto mode (m^*, n^*, p^*) must approach zero when f approaches $f_{m^*n^*p^*}$. This phenomenon has been investigated in [21, 22]. Moreover, a robust method of moments scheme is developed in [21] to avoid the numerical singularities when f is around $f_{m^*n^*p^*}$, which can be readily employed to obtain the numerical solutions to integral equation (1).

According to our method of moments solutions, the contributions from \mathbf{J}_t and \mathbf{J}_r dominate in Eq. (5); to be more specific, the contributions from \mathbf{M}_t and \mathbf{M}_r are typically two orders weaker than those from \mathbf{J}_t and \mathbf{J}_r . As a result, the contributions from \mathbf{M}_t and \mathbf{M}_r can be neglected in Eq. (5), leading to

$$(\tilde{\mathbf{J}}_t)_{z,m^*n^*p^*} \cong -(\tilde{\mathbf{J}}_r)_{z,m^*n^*p^*}, \quad \text{when } f \rightarrow f_{m^*n^*p^*}. \quad (12)$$

The relationship in Eq. (12) is verified by a numerical example below. The transmitting probe is located at $(x_t = 20 \text{ cm}, y_t = 20 \text{ cm})$, the receiving probe is located at $(x_r = 80 \text{ cm}, y_r = 80 \text{ cm})$, both probes have a radius of $r_p = 0.6 \text{ mm}$, and both probes have a length of $l_p = 17 \text{ cm}$. The operating frequency is $f = 424 \text{ MHz}$, which is very close to the resonant frequency of mode $(m^* = 2, n^* = 2, p^* = 0)$. A voltage source with $V_1 = 1 \text{ V}$ is applied at port 1 as the transmitter, and port 2 is terminated by a $50\text{-}\Omega$ load as the receiver. Simulation results of current distributions over the two probes, $I_t(z) = 2\pi r_p \mathbf{J}_t(z) \cdot \hat{\mathbf{z}}$ and $I_r(z) = 2\pi r_p \mathbf{J}_r(z) \cdot \hat{\mathbf{z}}$, are plotted in Figure 3. Apparently, $\mathbf{J}_t \cong -\mathbf{J}_r$. It is noted that the transmitting probe and receiving probe are symmetric to each other as far as mode $(m^* = 2, n^* = 2, p^* = 0)$ is concerned. Specifically, $\sin(k_{x,m^*}x_t) \sin(k_{y,n^*}y_t)$ and $\sin(k_{x,m^*}x_r) \sin(k_{y,n^*}y_r)$ have identical values. Moreover, the two probes share the same length and same radius. Due to Eqs. (10) and (11), it is fairly straightforward that Equation (12) holds true. Because the current at port 1, I_1 , is $I_t(z = 0)$ and the current at port 2, I_2 , is $I_r(z = 0)$, Figure 3 further reveals that $I_1 = -I_2$ approximately.

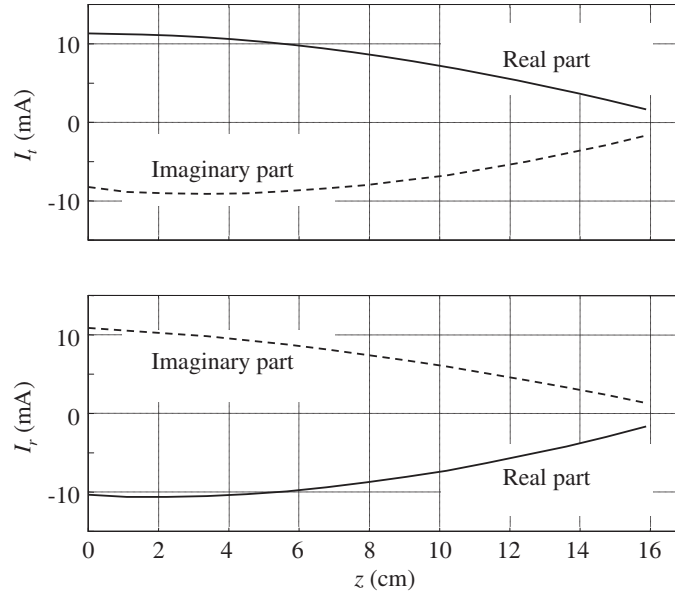


Figure 3. Simulation results of current distributions over probes with $(x_t = 20 \text{ cm}, y_t = 20 \text{ cm})$ and $(x_r = 80 \text{ cm}, y_r = 80 \text{ cm})$ at 424 MHz, the resonant frequency of mode TM_{z220} .

If I_1 and I_2 are both real-valued, “ $I_1 = -I_2$ ” results in 100% power transmission efficiency from port 1 to port 2. The proof is as follows. Because port 2 is terminated by a $50\text{-}\Omega$ load, the voltage at port 2 is $V_2 = -(50\ \Omega) \times I_2$. If there is no power loss over the cavity walls or over the cavity interior, $\text{Re}\{V_1 \cdot \text{conj}(I_1)\} = -\text{Re}\{V_2 \cdot \text{conj}(I_2)\}$ (here, the operator “conj” stands for “complex conjugate”). Then because of “ $I_1 = -I_2$,” V_1/I_1 is $50\ \Omega$, meaning that the load impedance is mapped to the transmitter side without any distortion. The reflection coefficient at port 1 with respect to the standard $50\text{-}\Omega$ is zero. Since there is no return loss at port 1 and the cavity is lossless, all the power is delivered from the transmitter to the receiver, in other words, the power transmission efficiency is 100%.

In Figure 3, the imaginary parts of I_1 and I_2 are on the same order of the real parts. As a result, the power transmission efficiency is considerably close to 100% though it is not exactly 100%. Specifically, $I_1 = (11.27 - j8.33)$ mA. The input impedance at port 1 is $V_1/I_1 = (57.4 + j42.4) \Omega$. The corresponding reflection coefficient at port 1 is $S_{11} = 0.19 + j0.32$, the return loss is $|S_{11}|^2 = 0.14$, and the power transmission efficiency is $|S_{21}|^2 = 1 - |S_{11}|^2 = 0.86 = 86\%$. From the numerical results, we find that the

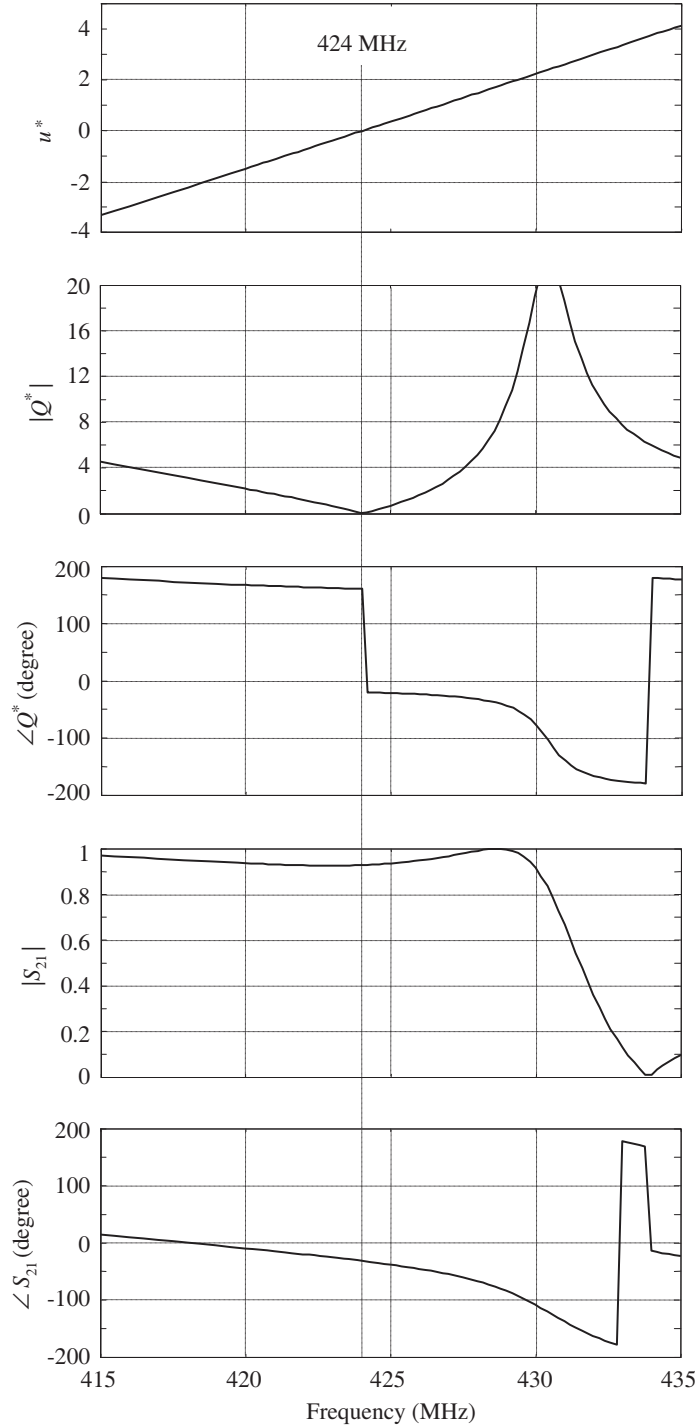


Figure 4. Numerical results with $(x_t = 20$ cm, $y_t = 20$ cm) and $(x_r = 80$ cm, $y_r = 80$ cm) around 424 MHz, the resonant frequency of mode TM_{z220} .

imaginary parts of I_1 and I_2 can be effectively controlled by l_p , and unsurprisingly, the imaginary parts of I_1 and I_2 are close to zero when $l_p \cong \lambda_0/4$, with $\lambda_0 = 2\pi/k$ denoting the wavelength in free space.

Figure 4 displays numerical results when the frequency f varies around 424 MHz. When $f = 424$ MHz, $u^* \cong 0$, $Q^* \cong 0$, and $|S_{21}| = 0.93$, as shown in the several paragraphs above. When f drops from 424 MHz to 415 MHz, $|Q^*|$ (amplitude of Q^*) changes so slightly that $|S_{21}|$ remains greater than 0.9 (corresponding to power transmission efficiency greater than 80%). When f drops from 424 MHz to 415 MHz, $\angle Q^*$ (phase of Q^*) increases slowly. As indicated by (5), Q^* embodies the “difference” between I_t and I_r . As $\angle Q^*$ changes slowly, $\angle S_{21}$ (phase of S_{21}) changes slowly as well in the frequency band of [415 MHz, 424 MHz]. When f increases from 424 MHz, $|Q^*|$ changes slowly initially and $|S_{21}|$ remains greater than 0.9 till frequency 430 MHz. Beyond 430 MHz, $|Q^*|$ changes drastically and $|S_{21}|$ becomes poor. We believe that the drastic change is because of the interference from mode ($m = 2, n = 2, p = 1$), whose resonant frequency resides at 450 MHz. In other words, the frequency band [430 MHz, 435 MHz] in Figure 4 is impacted by two modes heavily: mode ($m = 2, n = 2, p = 0$) and mode ($m = 2, n = 2, p = 1$). Whereas in frequency band [415 MHz, 430 MHz], mode ($m = 2, n = 2, p = 0$) dominates, as 367 MHz is the nearest resonant frequency (associated with mode ($m = 2, n = 1, p = 1$)) to the left of 424 MHz. The curve of $\angle Q^*$ has a 180-degree phase jump at frequency 424 MHz, because u^* changes its sign across 424 MHz. When f increases from 424 MHz to 430 MHz, $\angle Q^*$ and $\angle S_{21}$ both decrease smoothly. Overall within the frequency band [415 MHz, 430 MHz], $|S_{21}|$ is close to 1 and $\angle S_{21}$ appears linear with respect to frequency. It implies that the frequency band [415 MHz, 430 MHz] could be taken advantage of to achieve efficient wireless communication as well as wireless power transmission.

Before the end of this section, another numerical example is presented. Compared with the previous example, the only difference is that the receiving probe is located at ($x_r = 90$ cm, $y_r = 60$ cm). As the transmitting probe stays at location ($x_t = 20$ cm, $y_t = 20$ cm), the transmitting probe and receiving probe are no longer symmetric to each other with respect to mode ($m^* = 2, n^* = 2, p^* = 0$). Specifically,

$$\frac{\sin(k_{x,m^*}x_t)\sin(k_{y,n^*}y_t)}{\sin(k_{x,m^*}x_r)\sin(k_{y,n^*}y_r)} = \alpha = 2.62. \quad (13)$$

Simulation results of current distributions at 424 MHz over the two probes, $I_t(z)$ and $I_r(z)$, are plotted

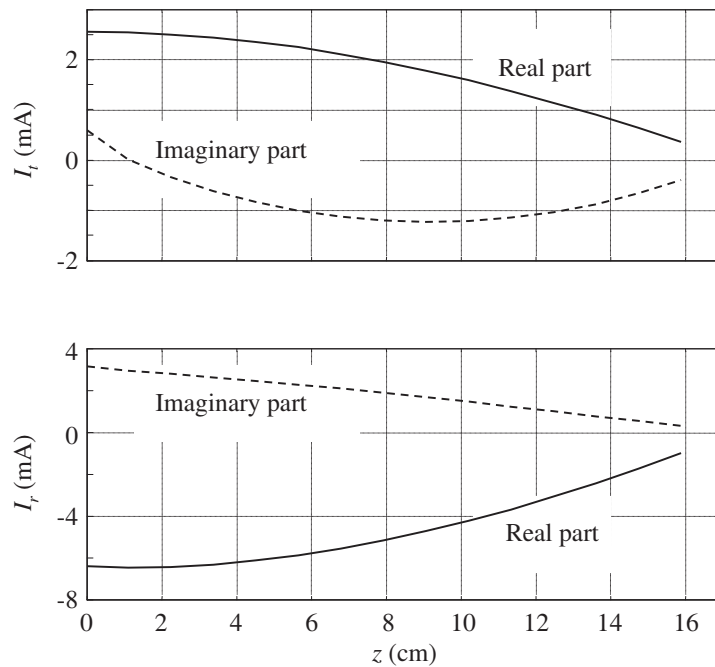


Figure 5. Simulation results of current distributions over probes with ($x_t = 20$ cm, $y_t = 20$ cm) and ($x_r = 90$ cm, $y_r = 60$ cm) at 424 MHz, the resonant frequency of mode TM_{z220} .

in Figure 5. It is observed that $\mathbf{J}_t \cong -\mathbf{J}_r/\alpha$, which makes Equation (12) valid. In the previous example, the value of α is 1; as a result, the load of port 2 is mapped to port 1 with little distortion and the return loss at port 1 is minimal. In this example, the load of port 2 is mapped to port 1 with a factor of

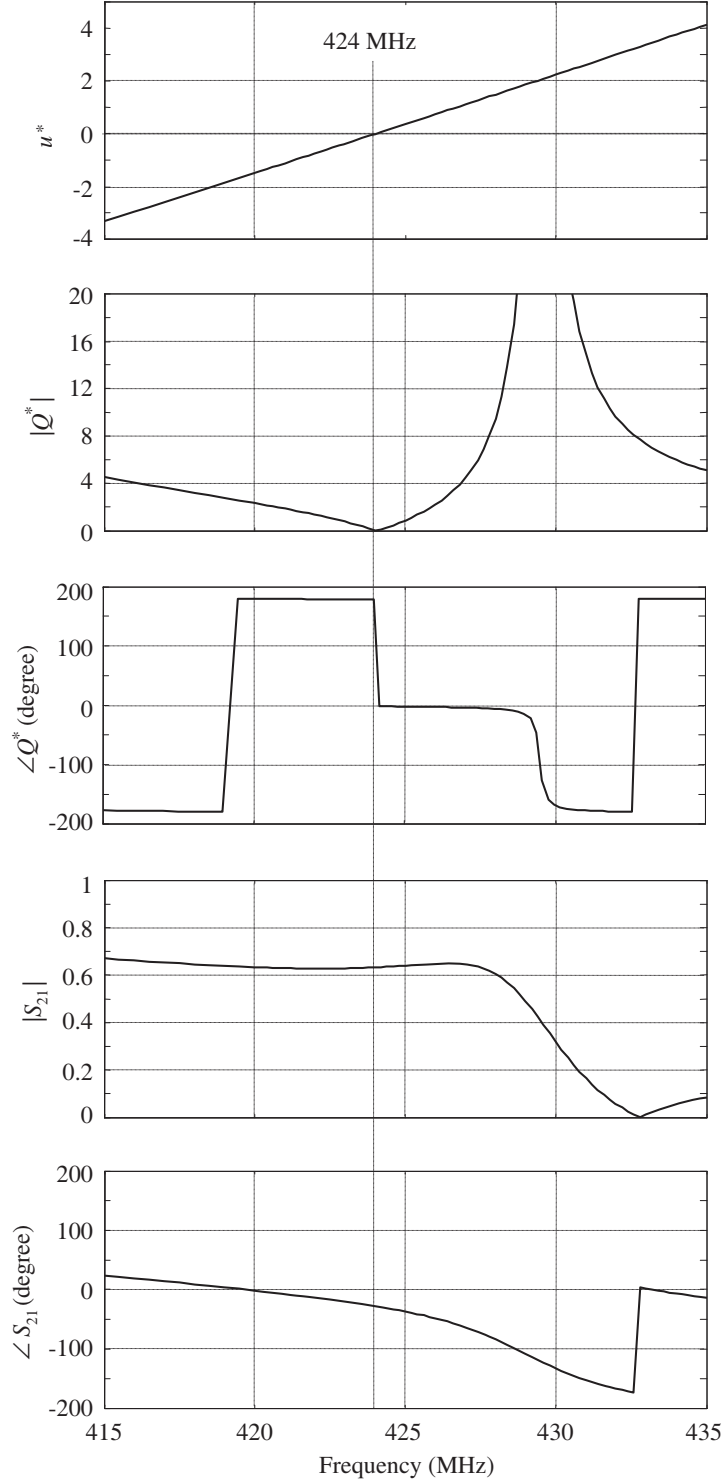


Figure 6. Numerical results with $(x_t = 20 \text{ cm}, y_t = 20 \text{ cm})$ and $(x_r = 90 \text{ cm}, y_r = 60 \text{ cm})$ around 424 MHz, the resonant frequency of mode TM_{z220} .

$\alpha = 2.62$; as a result, there is impedance mismatching at port 1, the return loss at port 1 is $|S_{11}|^2 = 0.6$, and the power transmission efficiency is $|S_{21}|^2 = 1 - |S_{11}|^2 = 0.4 = 40\%$.

Numerical results when the frequency f varies around 424 MHz are displayed in Figure 6. The phenomena in Figure 6 are similar to those of Figure 4, except that $|S_{21}|$ in Figure 6 has smaller values. Though the $|S_{21}|$ curve of Figure 6 is lower than the $|S_{21}|$ curve of Figure 4, it is flat between 415 MHz and 430 MHz. Meanwhile, the $\angle S_{21}$ curve of Figure 6 is linear with respect to the frequency between 415 MHz and 430 MHz. Therefore, the S_{21} 's behavior within frequency band [415 MHz, 430 MHz] in Figure 6 appears to be an excellent channel for wireless communication. Obviously, this channel is not optimal for wireless power transmission, since $|S_{21}|$ is not close to 1. As analyzed above, the small $|S_{21}|$ values of Figure 6 are due to the impedance mismatching at port 1, which is further due to factor α . Therefore, wireless power transmission is possible, subject to a matching network that is able to correct the mismatching due to factor α .

Though $(m^* = 2, n^* = 2, p^* = 0)$ is assumed throughout this section, the modal analysis in this section remains valid when (m^*, n^*, p^*) take other values. Therefore, it seems possible to identify wireless channels with properties similar to those in Figures 3 to 6 in other frequency bands as well. Some experimental results associated with $(m^* = 2, n^* = 2, p^* = 0)$, $(m^* = 3, n^* = 1, p^* = 0)$, and $(m^* = 3, n^* = 1, p^* = 1)$ are presented in Section 3.

3. EXPERIMENTAL VERIFICATIONS

In order to verify the modal analysis in Section 2, experiments are carried out within a cubic box as shown by a photo in Figure 7. In Figure 7, the z axis is pointing downward to facilitate routing the

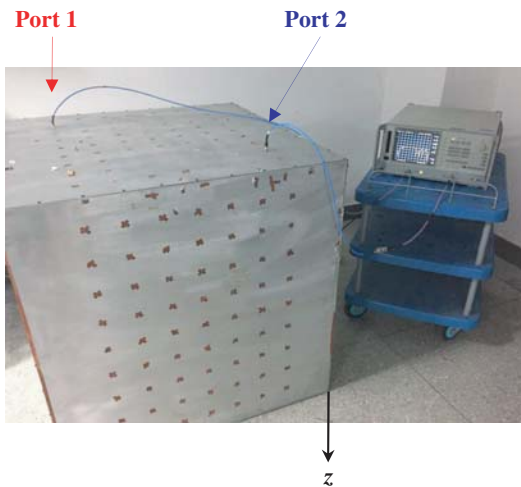


Figure 7. Photo of the experimental setup.

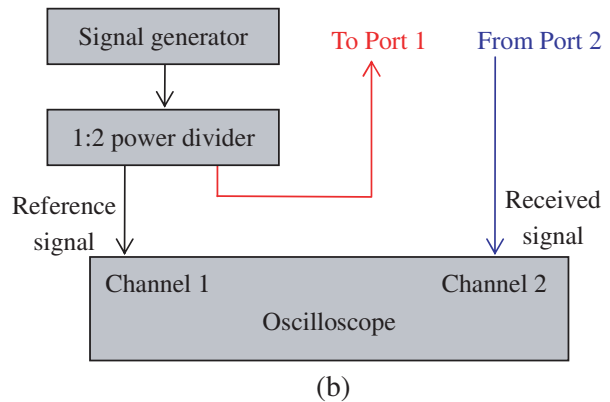
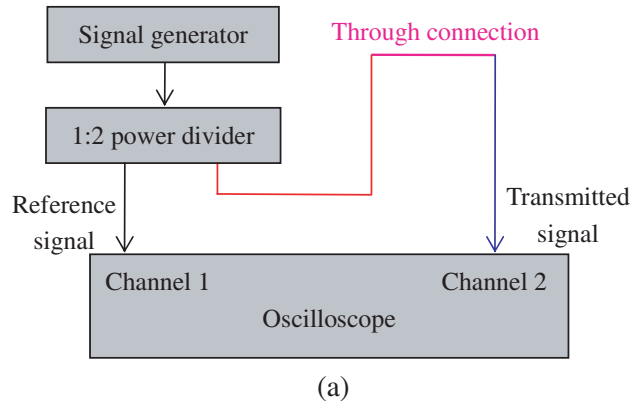


Figure 8. Procedure of the time domain measurement. (a) Measurement of the transmitted signal. (b) Measurement of the received signal.

cables. The six walls of the box are made of aluminum sheets with dimensions of approximately 1 meter by 1 meter and a thickness of roughly 2 mm. Because the aluminum sheets' dimensions are not 1 meter by 1 meter exactly and because of the aluminum sheets' thickness, the cavity is not perfectly cubic and its dimensions are slightly smaller than 1 cubic meter. To be specific, the cavity dimensions in experiments are $(0.986 \text{ m}) \times (0.986 \text{ m}) \times (0.981 \text{ m})$. Compared with the results in Section 2, the spectral results in this section shift toward positive frequency axis slightly; for instance, the resonant frequency associated with TM_{z220} mode is 424 MHz in Section 2, whereas it is 430 MHz in this section. The slightly smaller dimensions in practice do not generate any other significant impacts. There are one transmitting probe and one receiving probe in the cavity, both made of thin copper wires. Port 1 and port 2 are defined at the co-axial connectors connected to the transmitting probe and receiving probe, respectively.

Measurements are conducted in the frequency domain as well as time domain. In the frequency domain, scattering parameter S_{21} is measured between port 1 and port 2 by a network analyzer manufactured by Radasun Instruments with model number AV3620A. The procedure of the time domain measurement is depicted in Figure 8. A pulse train is generated by a signal generator manufactured by Rigol with model number DSG3060. The pulse train is fed to a 1 : 2 power divider manufactured by Pulsar with model number P2-17-411; the two outputs of the power divider are assumed to be identical to each other. One output of the power divider is recorded by channel 1 of an oscilloscope as "reference signal." When the other output of the power divider is directly recorded by channel 2 of the oscilloscope, the signal measured at channel 2 is "transmitted signal," as shown in Figure 8(a). When the other output of the power divider is fed to port 1 and when the signal at port 2 is recorded by channel 2 of the oscilloscope, the signal measured at channel 2 is "received signal," as shown in Figure 8(b). With "reference signal" as the temporal reference, the difference between "transmitted signal" and "received signal" characterizes the wireless channel in the fully-enclosed cavity. The oscilloscope used in our experiments are manufactured by Rigol with model number MSO4054; in all the measurements of this section, its temporal sampling rate is fixed to be 4 Giga samples per second.

Three wireless channels within the cubic cavity are measured in this section, as depicted in Figure 9. In all the experiments, the transmitting probe's location is fixed. Channel A, channel B, and channel C are defined between the transmitting probe and receiving probe when the receiving probe is at location A, location B, and location C, respectively.

Measurement results around 430 MHz, the resonant frequency of TM_{z220} mode in the cubic cavity,

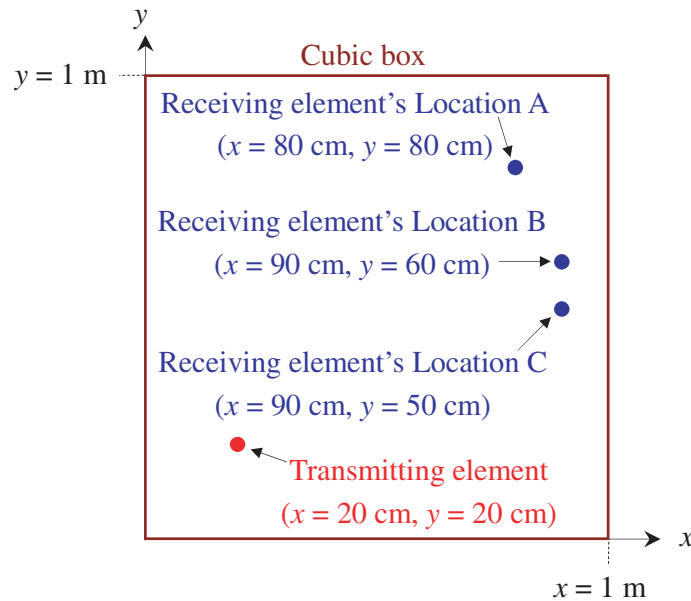


Figure 9. Depiction of the three channels characterized in Section 3.

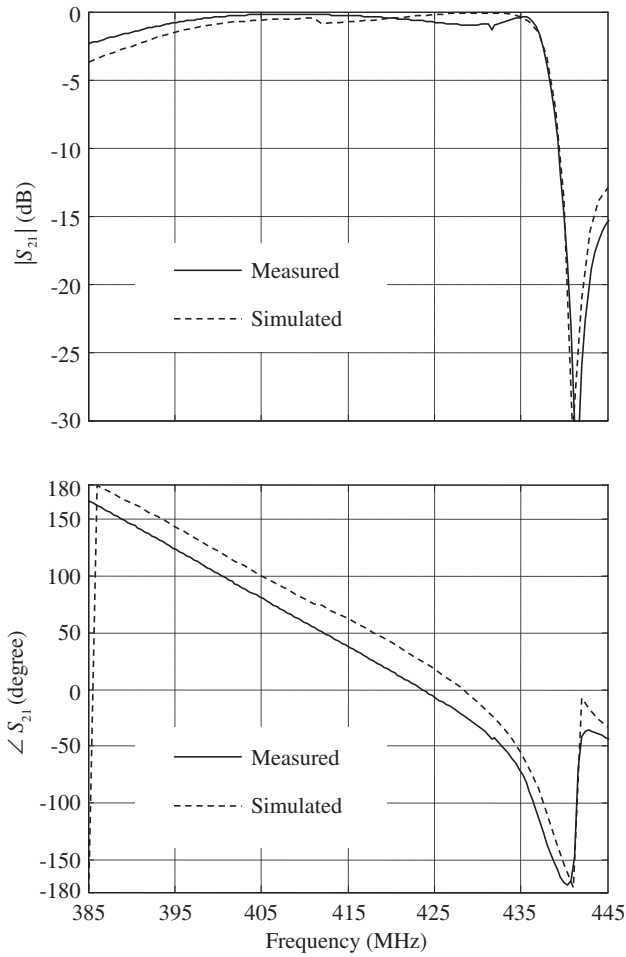


Figure 10. Frequency domain measurement and simulation results of channel A (with receiver at bright spot) around 430 MHz, the resonant frequency of mode TM_{z220} .

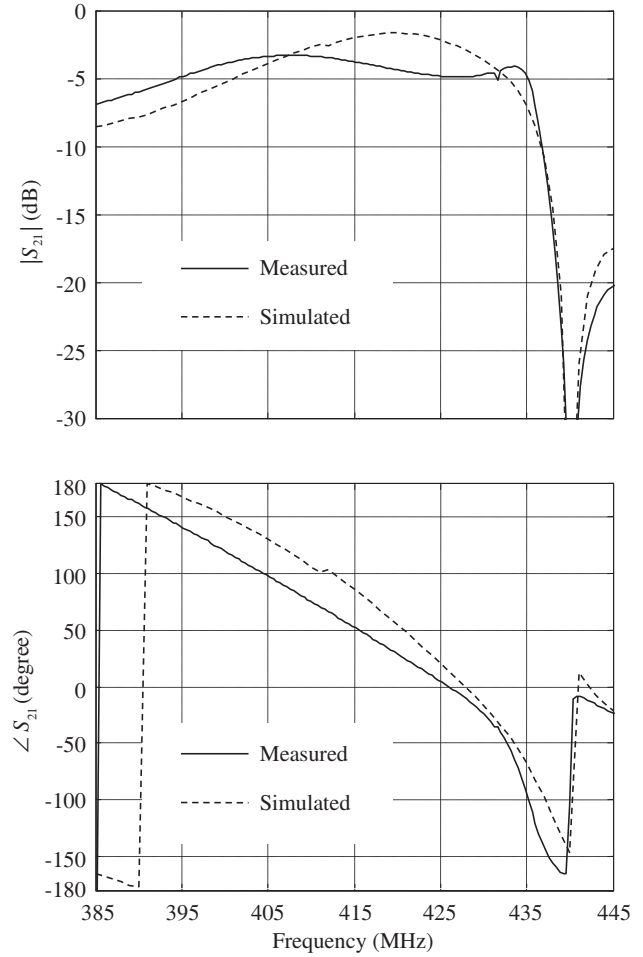


Figure 11. Frequency domain measurement and simulation results of channel B (with receiver at medium spot) around 430 MHz, the resonant frequency of mode TM_{z220} .

are presented in Figures 10 to 15 in order to verify the theoretical results in Section 2. Both the transmitting probe and receiving probe have a length of $l_p = 17$ cm in Figures 10 to 15.

Measured S_{21} data around 430 MHz are plotted in Figures 10, 11, and 12, which correspond to channel A, channel B, and channel C respectively. In Figure 10, the magnitude of S_{21} , $|S_{21}|$, is fairly flat between 395 MHz and 435 MHz. Meanwhile between 395 MHz and 435 MHz, the curve of $\angle S_{21}$, phase of S_{21} , in Figure 10 is linear with respect to frequency. The slope associated with the $\angle S_{21}$ curve in frequency band [395 MHz, 435 MHz] indicates a group delay of 11.77 ns. Thus, channel A appears to be an excellent wireless communication channel between 395 MHz and 435 MHz. The $|S_{21}|$ curve of Figure 11 is fairly flat between 395 MHz and 435 MHz, but with smaller values than Figure 10. The $|S_{21}|$ curve of Figure 12 is even lower. The $|S_{21}|$ data in Figures 10, 11, and 12 can be interpreted by the standing wave pattern. Around 430 MHz, TM_{z220} mode is the dominant mode inside the cubic cavity. The magnitude of E_z field of TM_{z220} mode reaches peak value at $(x = 75$ cm, $y = 75$ cm); thus, location A represents a “bright spot” for the receiver. The magnitude of E_z field of TM_{z220} mode is zero when $x = 50$ cm; thus, location C is a “dark spot” for the receiver. As a scenario between location A and location C, location B is termed a “medium spot” for the receiver. The similarity among $\angle S_{21}$ data of Figures 10, 11, and 12 is reasonable, because TM_{z220} mode dominates around 430 MHz and all the locations inside the cubic cavity share the same phase as far as TM_{z220} mode is concerned. It is noted that channel A can be employed for wireless power transmission as well as wireless communication, as its

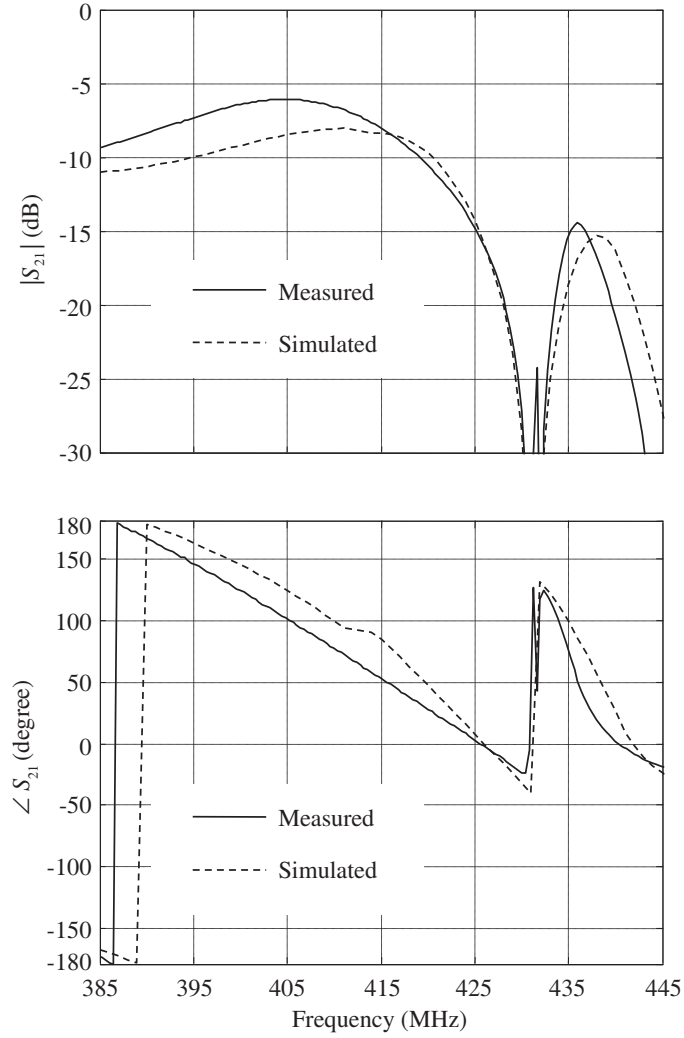


Figure 12. Frequency domain measurement and simulation results of channel C (with receiver at dark spot) around 430 MHz, the resonant frequency of mode TM_{z220} .

$|S_{21}|$ is greater than -1.5 dB (corresponding to power transmission efficiency greater than 70%) between 395 MHz and 435 MHz. As analyzed in Section 2, the poor power transmission efficiencies of channel B and channel C are attributed to impedance mismatching. With appropriate matching networks, it may be possible to employ channel B and channel C for wireless power transmission, too. In Figures 10, 11, and 12, simulation results based on the modal analysis in Section 2 match the measurement results very well, indicating that the proposed modal analysis is capable of predicting the characteristics of practical wireless channels in fully-enclosed environments.

Time domain measurement results around 430 MHz are plotted in Figures 13, 14, and 15. With the measured S_{21} data as guideline, the pulses generated by the signal generator are tailored to have frequency coverage roughly between 395 MHz and 435 MHz. The time domain results in Figure 13 are consistent with the frequency domain results in Figure 10. The received pulses' temporal width is not broadened compared with the transmitted pulses in Figure 10, as the $\angle S_{21}$ curve in Figure 10 exhibits little dispersion between 395 MHz and 435 MHz. The time delay between an individual transmitted pulse and its counterpart of the received pulse train is between 11 ns and 12 ns, which matches the slope of $\angle S_{21}$ in Figure 10. Because $|S_{21}|$ approaches 1 between 395 MHz and 435 MHz in Figure 10, in Figure 13 the received pulses have almost the same amplitude as the transmitted pulses. In order to visualize the signals clearly, the pulse repetition interval is as large as 200 ns in Figure 13. The pulses in

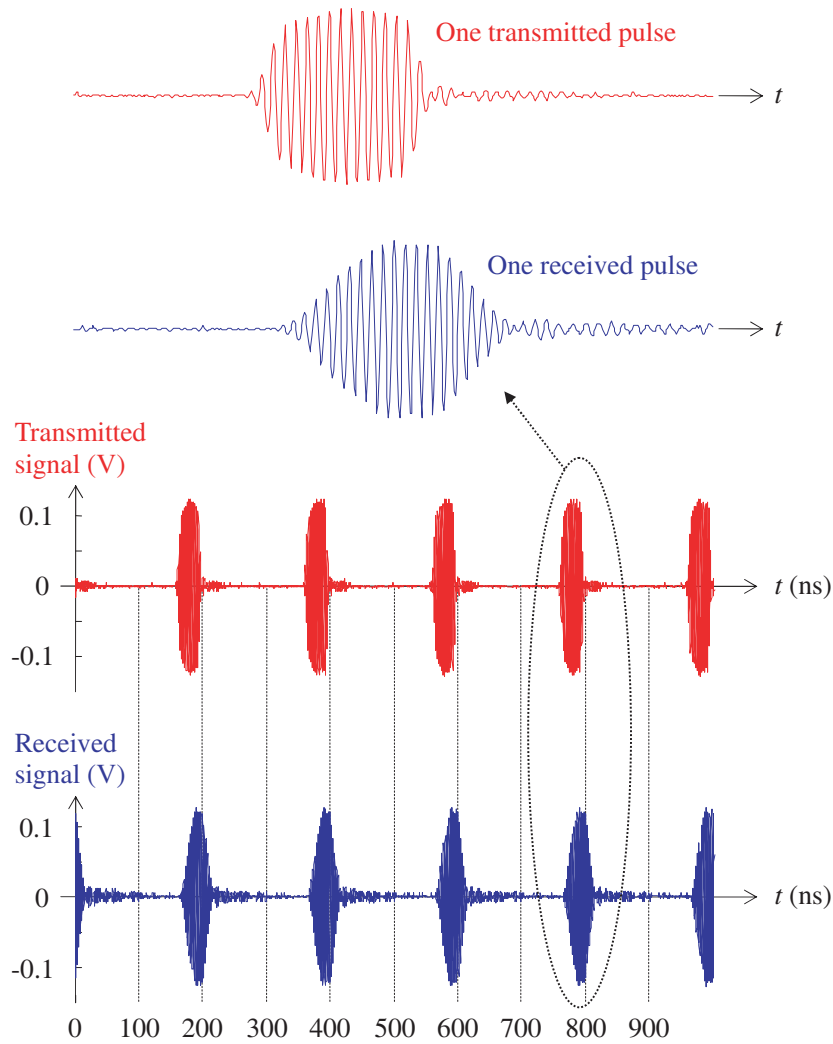


Figure 13. Time domain measurement results of channel A (with receiver at bright spot) around 430 MHz, the resonant frequency of mode TM_{z220} .

the received signal could be easily differentiated among one another in time when the pulse repetition interval is reduced to 50 ns. If each pulse stands for one bit, it appears readily feasible for channel A to accommodate wireless communication with data rate of at least 20 Mbps (which corresponds to 50 ns pulse repetition interval). It should be noted that data rate on the order of Mbps is very difficult to accomplish in fully-enclosed environments (according to [3–12], for instance), whereas 20 Mbps may not be considered a high data rate in regular environments. The phenomena displayed in Figure 14 and Figure 15 are similar to those in Figure 13, except that the received pulses have weaker amplitudes in Figure 14 and Figure 15. From the results of Figure 15, it seems that high-speed wireless communication is possible even when the receiver is located at a “dark spot.”

Overall, the experimental results in Figures 10 to 15 agree with the modal analysis results in Section 2 very well. Both theoretical and experimental results demonstrate excellent wireless channels around the resonant frequency associated with TM_{z220} mode. As the modal analysis in Section 2 appears to be applicable to other cavity modes as well, we are motivated to seek channels with similar properties in other frequency bands. Two sets of experimental results are presented in Figure 16 and Figure 17, which are associated with the TM_{z310} mode and TM_{z311} mode respectively.

The experimental and numerical results in Figure 16 are obtained around the frequency of 481 MHz, the resonant frequency associated with the TM_{z310} mode. The transmitting probe is located at

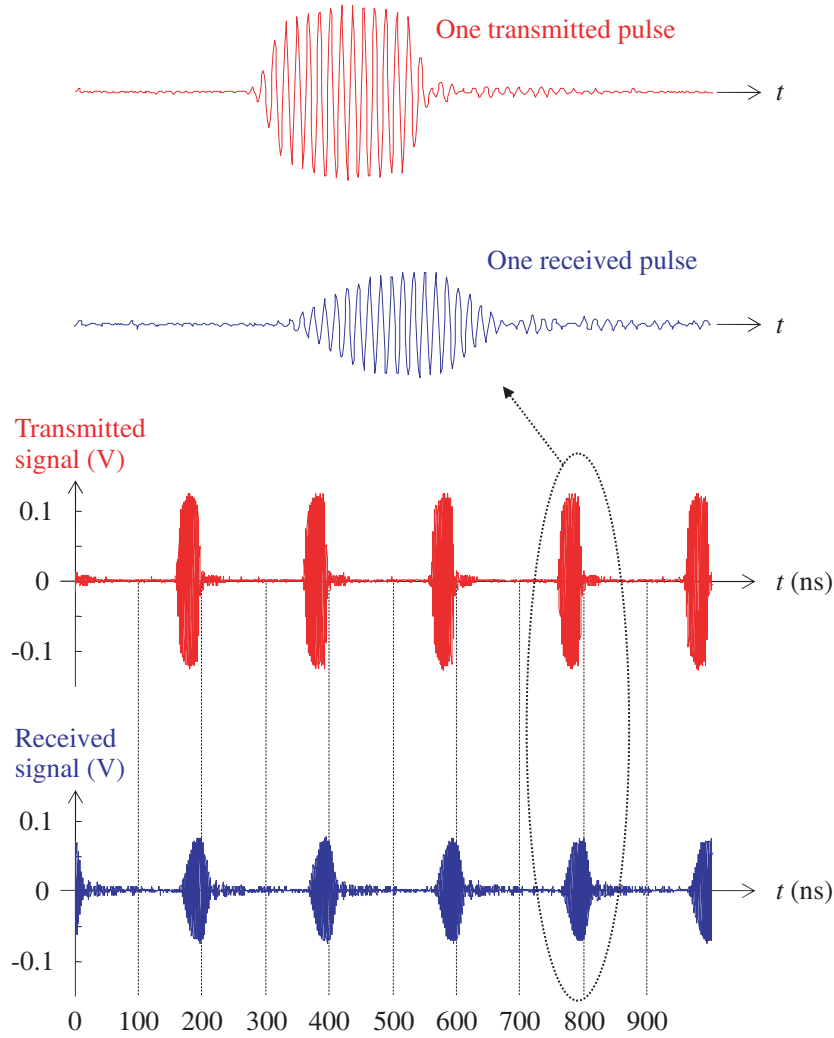


Figure 14. Time domain measurement results of channel B (with receiver at medium spot) around 430 MHz, the resonant frequency of mode TM_{z220} .

($x_t = 20$ cm, $y_t = 20$ cm), and the receiving probe is located at ($x_r = 80$ cm, $y_r = 80$ cm); in other words, channel A depicted in Figure 9 is characterized. Both the transmitting probe and receiving probe have a length of $l_p = 14.6$ cm $\cong \lambda_0/4$, with λ_0 corresponding to frequency 481 MHz. The wireless channel portrayed in Figure 16 has similar properties to the channel in Figure 10. Specifically, $|S_{21}|$ is close to 1, and the curve of $\angle S_{21}$ is linear with respect to frequency between 480 MHz and 490 MHz. Apparently, the 10-MHz bandwidth in Figure 16 is limited by the two neighboring modes, TM_{z221} (with resonant frequency 457 MHz) and TM_{z311} (with resonant frequency 505 MHz). The channel in Figure 16 appears an excellent candidate for wireless communication as well as wireless power transmission.

The experimental and numerical results in Figure 17 are obtained around frequency 505 MHz, the resonant frequency associated with the TM_{z311} mode. The transmitting probe is located at ($x_t = 20$ cm, $y_t = 20$ cm), and the receiving probe is located at ($x_r = 80$ cm, $y_r = 80$ cm). Both the transmitting probe and receiving probe have a length of $l_p = 13.4$ cm $\cong \lambda_0/4$, with λ_0 corresponding to frequency 505 MHz. Obviously, $|S_{21}|$ is close to 1, and the curve of $\angle S_{21}$ is linear with respect to frequency between 500 MHz and 520 MHz, i.e., with bandwidth of roughly 20 MHz. The channel in Figure 17 appears applicable to both wireless communication applications and wireless power transmission applications.

The experimental results in this section as well as the theoretical results in Section 2 indicate that each cavity mode might be able to support excellent wireless channels, but the wireless channels become

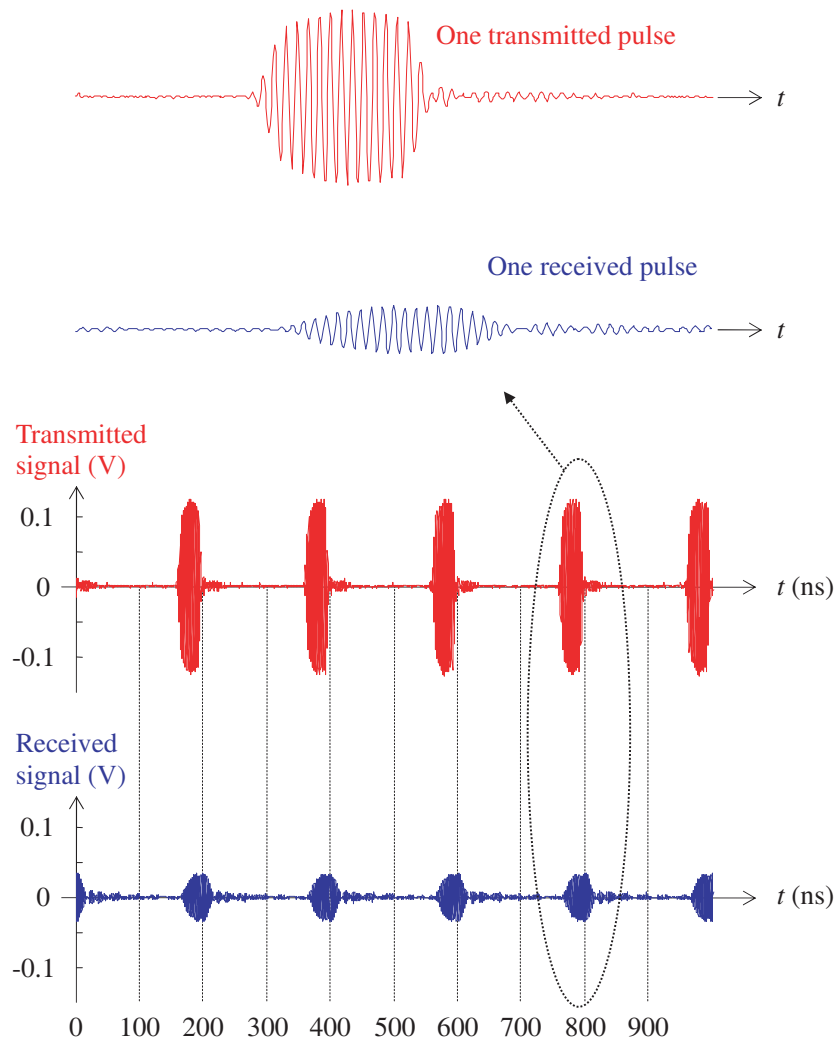


Figure 15. Time domain measurement results of channel C (with receiver at dark spot) around 430 MHz, the resonant frequency of mode TM_{z220} .

explicit only when one cavity mode dominates. In other words, the channel properties associated with one mode would be interfered by another mode whose resonant frequency is adjacent. With the increase of the mode order, the resonant frequencies of cavity modes are more and more densely populated (asymptotic relationship between mode density and frequency is given in [23]). Thus, it would be difficult to identify wireless channels associated with high-order modes. As a benefit of studying low-order modes, their resonant frequencies are low such that ohmic loss can be ignored in the modal analysis of this paper. To be specific, the modes investigated in this paper (such as 220, 310, and 311 modes) have resonant frequencies lower than 1 GHz. The ohmic loss over cavity walls is not significant below 1 GHz, as the experimental results in Section 3 demonstrate power transmission efficiencies close to 100%. However, it is also observed from our measurements that the ohmic loss is not negligible beyond 1 GHz; in other words, beyond 1 GHz experimental data exhibit large discrepancy with the modal analysis results. We are currently applying impedance boundary conditions to characterize the cavity walls in order to incorporate ohmic loss into the modal analysis beyond 1 GHz. Generally speaking, ohmic loss would decrease the quality factor and in turn would benefit the bandwidth of wireless communication. However meanwhile, ohmic loss would degrade the efficiency of wireless power transmission. We will report our research outcomes on the impact of ohmic loss in subsequent publications.

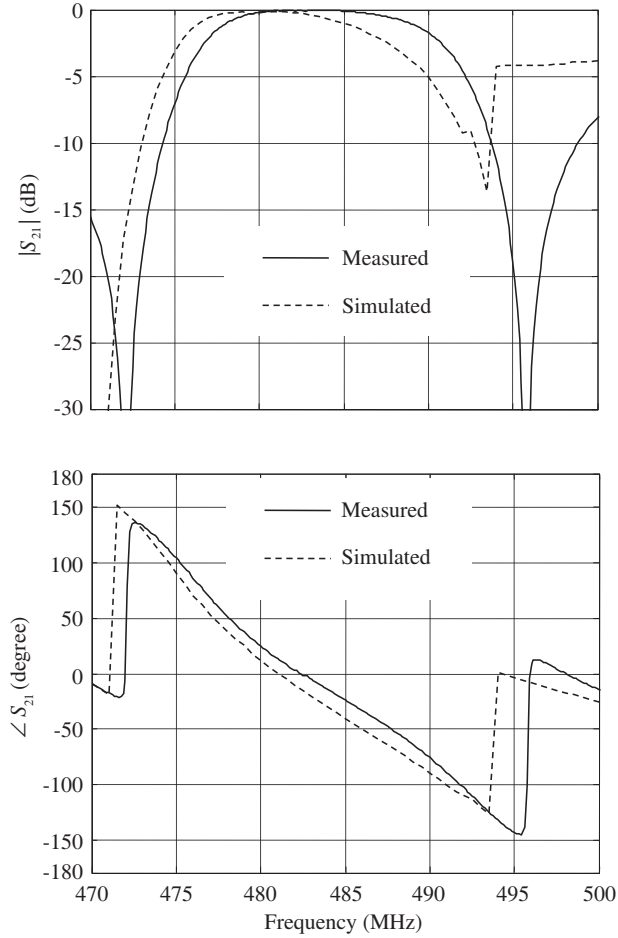


Figure 16. Frequency domain measurement and simulation results of channel A around 481 MHz, the resonant frequency of mode TM_{z310} .

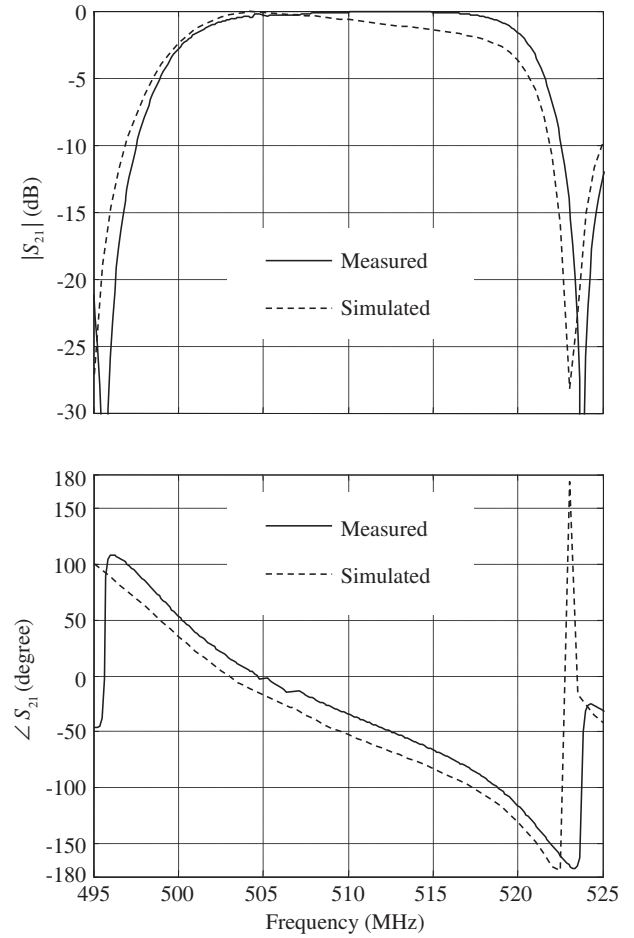


Figure 17. Frequency domain measurement and simulation results of channel A around 505 MHz, the resonant frequency of mode TM_{z311} .

4. CONCLUSIONS

This paper reports a semi-analytical modal analysis scheme based on an integral equation method, which is applied to characterize wireless channels in a cubic cavity with a side length of 1 meter. The analysis results reveal that when a transmitter and a receiver are symmetric to each other as far as TM_{220} mode is concerned, the load of the receiver could be mapped to the transmitter with little distortion, leading to excellent wireless channels with the potential of accomplishing efficient wireless communication and/or wireless power transmission. The theoretical analysis further indicates that each cavity mode is able to support excellent wireless channels, whereas the channels become explicit only when one cavity mode dominates. The modal analysis is verified by experiments in the frequency domain as well as time domain. Excellent wireless communication channels approximately between 395 MHz and 435 MHz, that is, with an absolute bandwidth as large as 40 MHz, are demonstrated. Based on the measurement data, these channels have the potential of accommodating wireless communication with data rate of at least 20 Mbps. The power transmission efficiency is greater than 70% within frequency band [395 MHz, 435 MHz] when the receiver is located at certain “bright spots.” At certain “dark spots,” the receiver receives little power but wireless communication with data rate of 20 Mbps still appears feasible. Two other excellent wireless channels are also demonstrated by measurements as predicted by the modal analysis: one associated with the TM_{310} mode with 10 MHz bandwidth, and one associated with the TM_{311} mode with 20 MHz bandwidth.

ACKNOWLEDGMENT

This work was supported in part by the National Natural Science Foundation of China Grant 61871220, National Natural Science Foundation of China Grant 61628106, and National Science Foundation Grant ECCS 1503600.

REFERENCES

1. Barton, R. J., S. W. Raymond, and W. F. Patrick, "Space applications of low-power active wireless sensor networks and passive RFID tags," *Wireless Sensor and Mobile Ad-Hoc Networks*, D. Benhaddou and A. Al-Fuqaha (eds.), 97–127, Springer, New York, 2015.
2. Wu, J., J. Liang, X. Wang, C. Chen, X. Zhang, and M. Lu, "Feasibility study of efficient wireless power transmission in satellite interior," *Microwave and Optical Technology Letters*, Vol. 58, No. 10, 2518–2522, October 2016.
3. Panitz, M. and D. C. Hope, "Characteristics of wireless systems in resonant environments," *IEEE Electromagnetic Compatibility Magazine*, Vol. 3, No. 3, 64–75, October 2014.
4. Hope, D. C., "Towards a wireless aircraft," Ph.D. dissertation, University of York, United Kingdom, 2011.
5. Centeno, A. and N. Alford, "Measurement of ZigBee wireless communications in mode-stirred and mode-tuned reverberation chamber," *Progress In Electromagnetics Research M*, Vol. 18, 171–178, 2011.
6. Hope, D., J. Dawson, A. Marvin, M. Panitz, C. Christopoulos, and P. Sewell, "Assessing the performance of ZigBee in a reverberant environment using a mode stirred chamber," *IEEE International Symposium on Electromagnetic Compatibility*, Detroit, Michigan, August 2008.
7. Panitz, M., C. Christopoulos, P. Sewell, D. Hope, J. Dawson, and A. Marvin, "Modelling wireless communication in highly-multipath low-loss environments," *The International Symposium on Electromagnetic Compatibility — EMC Europe*, Hamburg, Germany, September 2008.
8. Van't Hof, J. P. and D. D. Stancil, "Wireless sensors in reverberant enclosures: Characterizing a new radio channel," *IEEE 62nd Vehicular Technology Conference*, Dallas, Texas, September 2005.
9. Hwu, S. U., B. A. Rhodes, B. Kanishka deSilva, C. C. Sham, and J. R. Keiser, "RF exposure analysis for multiple Wi-Fi devices in enclosed environment," *IEEE Sensors Applications Symposium*, Galveston, Texas, February 2013.
10. Recanatini, R., F. Moglie, and V. Mariani Primiani, "Performance and immunity evaluation of complete WLAN systems in a large reverberation chamber," *IEEE Transactions on Electromagnetic Compatibility*, Vol. 55, No. 5, 806–815, October 2013.
11. Konefal, T., J. F. Dawson, A. C. Denton, T. M. Benson, C. Christopoulos, A. C. Marvin, S. J. Porter, and D. W. P. Thomas, "Electromagnetic coupling between wires inside a rectangular cavity using multiple-mode-analogous-transmission-line circuit theory," *IEEE Transactions on Electromagnetic Compatibility*, Vol. 43, No. 3, 273–281, 2001.
12. Nanni, A., D. W. P. Thomas, C. Christopoulos, T. Konefal, J. Paul, L. Sandrolini, U. Reggiani, and A. Massarini, "Electromagnetic coupling between wires and loops inside a rectangular cavity using multi-mode transmission line theory," *International Symposium on Electromagnetic Compatibility — EMC Europe*, Eindhoven, The Netherlands, September 2004.
13. Chabalko, M. J. and A. P. Sample, "Resonant cavity mode enabled wireless power transfer," *Applied Physics Letters*, Vol. 105, No. 24, 243902, 2014.
14. Chabalko, M. J., M. Shahmohammadi, and A. P. Sample, "Quasistatic cavity resonance for ubiquitous wireless power transfer," *PLoS ONE*, Vol. 12, No. 2, e0169045, 2017.
15. Mei, H., K. A. Thackston, R. A. Bercich, J. G. R. Jefferys, and P. P. Irazoqui, "Cavity resonator wireless power transfer system for freely moving animal experiments," *IEEE Transactions on Biomedical Engineering*, Vol. 64, No. 4, 775–785, April 2017.

16. Korhummel, S., A. Rosen, and Z. Popovic, "Over-moded cavity for multiple-electronic-device wireless charging," *IEEE Transactions on Microwave Theory and Techniques*, Vol. 62, No. 4, 1074–1079, April 2014.
17. Chabalko, M. J. and A. P. Sample, "Three-dimensional charging via multi-mode resonant cavity enabled wireless power transfer," *IEEE Transactions on Power Electronics*, Vol. 30, No. 11, 6163–6173, November 2015.
18. Wang, X., C. Chen, H. Wong, and M. Lu, "A reconfigurable scheme of wireless power transmission in fully enclosed environments," *IEEE Antennas and Wireless Propagation Letters*, Vol. 16, 2959–2962, 2017.
19. Tsai, L. L., "A numerical solution for the near and far fields of an annular ring of magnetic current," *IEEE Transactions on Antennas and Propagation*, Vol. 20, No. 5, 569–576, September 1972.
20. Tai, C.-T. and P. Rozenfeld, "Different representations of dyadic Green's functions for a rectangular cavity," *IEEE Transactions on Microwave Theory and Techniques*, Vol. 24, No. 9, 597–601, September 1976.
21. Lu, M., J. W. Bredow, S. Jung, and S. Tjuatja, "Evaluation of Green's functions of rectangular cavities around resonant frequencies in the method of moments," *IEEE Antennas and Wireless Propagation Letters*, Vol. 8, 204–208, 2009.
22. Lu, M. and S. Jung, "On the well-posedness of integral equations associated with cavity Green's functions around resonant frequencies," *Microwave and Optical Technology Letters*, Vol. 51, No. 6, 1476–1481, June 2009.
23. Hill, D. A., *Electromagnetic Fields in Cavities: Deterministic and Statistical Theories*, 7–8, Wiley-IEEE Press, Hoboken, NJ, 2009.